We are IntechOpen,
the world's leading publisher of
Open Access books
Built by scientists, for scientists

4,800
Open access books available

122,000
International authors and editors

135M
Downloads

Our authors are among the

154
Countries delivered to

TOP 1%
most cited scientists

12.2%
Contributors from top 500 universities

WEB OF SCIENCE™

Selection of our books indexed in the Book Citation Index
in Web of Science™ Core Collection (BKCI)

Interested in publishing with us?
Contact book.department@intechopen.com

Numbers displayed above are based on latest data collected.
For more information visit www.intechopen.com

Indium Phosphide Bismide

Liyao Zhang, Wenwu Pan, Xiaoyan Wu, Li Yue and
Shumin Wang

Additional information is available at the end of the chapter

Abstract

Indium phosphide bismide is a new member to the dilute bismide family. Since the first synthesis by molecular beam epitaxy (MBE) in 2013, it has cut a figure for its abnormal properties comparing with other dilute bismides. Bismuth (Bi) incorporation is always a difficulty for epitaxial growth of dilute. In this chapter, it shows how to regulate MBE growth parameters and their influence on Bi incorporation in $InP_{1-x}Bi_x$. Structural, electronic and optical properties are systematically reviewed. Thermal annealing to study Bi thermal stability and its effect on physical properties is performed. $InP_{1-x}Bi_x$ shows strong and broad photoluminescence at room temperature, which is a potential candidate for fabricating super-luminescence diodes applied for enhancing spatial resolution in optical coherence tomography. Quaternary phosphide bismide, including InGaPBi and InAlPBi, is briefly introduced in this chapter.

Keywords: $InP_{1-x}Bi_x$, MBE, structure property, electronic property, optical property, thermal stability

1. Introduction

III–V compound semiconductor plays an important role in modern optoelectronic devices for its special physical properties whose band structure could be tailored to meet various device applications. While extensive researches on III-Vs have been carried out for over 60 years, bismuth (Bi) containing III-V-Bi is the least investigated compound. As GaAsBi was first successfully grown by metal organic vapour phase epitaxy (MOVPE) in 1998 [1] and by molecular beam epitaxy (MBE) in 2003 [2], people found several promising physical properties of various dilute bismides, which arouse an upsurge of research on these novel class III-Vs.

As Bi is the heaviest non-radioactive element, it is predicted [3, 4] that dilute bismides will get large spin-orbit splitting energy, which could suppress Auger recombination and improve the characteristic temperature of lasers fabricated with dilute bismide materials. When Bi is incorporated into III-Vs, Bi will form impurity levels close to the valence band (VB) of the host material [5]. If the incorporated Bi concentration increases from doping level to dilute alloy level, the Bi states will broaden and interact with the host valence band, which will cause band gap bowing effect [3]. The bandgap of InP is 1.35 eV at room temperature and will be reduced by about 106 meV for incorporating per 1% Bi [6]. This could help to regulate the material band gap, such as red shifting the bandgap to telecommunication band on GaAs, or even mid-infrared range on GaSb. Unlike dilute nitrides in which incorporating N atoms will significantly reduce the electron mobility and form a lot of non-radiative recombination centres, dilute bismides do not reduce the electron mobility for a small amount of Bi [7]. Bismuth could also act as a surfactant during III-V material growth [8], which makes the interface and/or surface much smoother, improving the optical properties of the materials.

Berding *et al*. predicted InSbBi, InAsBi and InPBi to be potential candidates for mid- and far-infrared optoelectronics application in 1988 [9]. Through a series of calculations, they pointed out that InPBi and InSbBi was the most difficult and the easiest to synthesize, respectively, because there was a larger miscibility gap in $InP_{1-x}Bi_x$ than that in the other two materials. However, once InPBi was successfully mixed, it would be the most robust among the three alloys.

$InP_{1-x}Bi_x$ was first successfully grown by MBE in our group in 2013 [10] and showed several special properties comparing with other dilute bismides, such as broad and strong photoluminescence (PL) at 1.4–2.7 μm at room temperature. This property makes $InP_{1-x}Bi_x$ very attractive for fabricating super-luminescence diodes applied in optical coherence tomography (OCT), which is a non-invasive painless diagnosis technique.

In this chapter, epitaxial growth and physical properties of $InP_{1-x}Bi_x$ and its quaternary compound InGaPBi and InAlPBi are summarized. The potential application in medical diagnosis is also described.

2. Epitaxial growth and characterization

$InP_{1-x}Bi_x$ is difficult to be synthesized as mentioned and has a narrow growth parameter window. The growth parameters, such as growth temperature, Bi flux, PH_3 pressure and growth rate, were investigated to optimize the $InP_{1-x}Bi_x$ crystal quality. $InP_{1-x}Bi_x$ epitaxial layers were grown on semi-insulating InP (100) substrates by V90 gas-source MBE (GSMBE). The beam equivalent pressure (BEP) of the In and Bi sources was measured by a retractable ion gauge. The fluxes of elemental In and Bi were controlled by adjusting the respective effusion cell temperatures while P_2 was cracked from PH_3 at 1000°C.

The growth temperature was decreased to about 275–364°C to initiate the growth of 250–420 nm thick $InP_{1-x}Bi_x$. High-resolution X-ray diffraction (HRXRD), atomic force microscopy

(AFM), energy dispersive X-ray spectroscopy (EDX), scanning electron microscope (SEM) and Rutherford backscattering spectroscopy (RBS) were used to characterize surface and structural properties of the $InP_{1-x}Bi_x$ thin films.

2.1. Effect of growth temperature

Growth temperature is a key parameter for growing dilute bismides as it directly affects the epi-growth process. In GSMBE technique for growth of $InP_{1-x}Bi_x$ alloys with smooth surface and good crystal quality, the optimized growth temperature is about 300–330°C. A set of samples with thickness of 420 nm labelled as A, B and C were grown by GSMBE at 275°C, 324°C and 364°C, respectively, all measured by a thermocouple. AFM result, as shown in **Figure 1(a)**, shows that In/Bi droplets appear in Sample A grown at 364°C with a density in the order of 10^7 cm^{-2} while smooth surface with a low root-mean-square (RMS) roughness value of only 1 nm can be achieved in Sample B when decreasing the growth temperature to 324°C. If the growth temperature is further lowered to 275°C, a whisker-like surface feature with a high RMS roughness value of 17 nm is observed in Sample C.
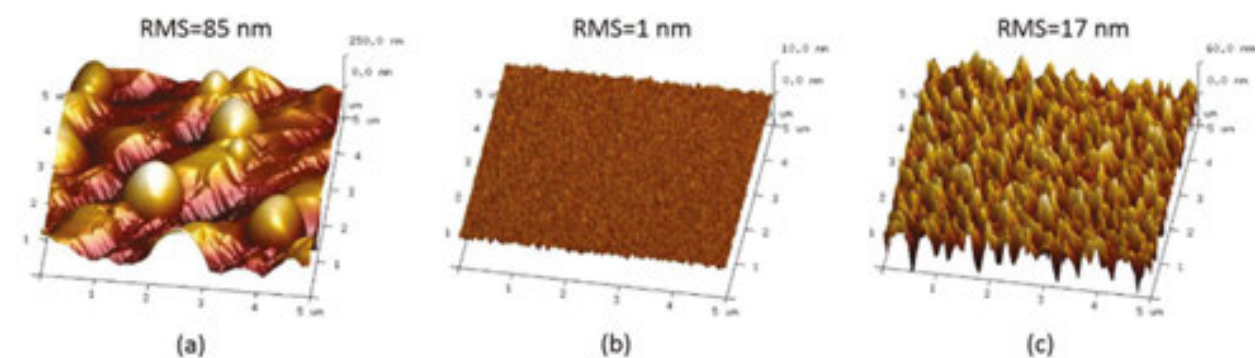

Figure 1. Surface morphology of InP(Bi) samples grown at (a) 364°C – Sample A, (b) 324°C – Sample B and (c) 275°C – Sample C.

Figure 2 shows HRXRD (004) ω/2θ rocking curves for the three samples. The left peak corresponds to the $InP_{1-x}Bi_x$ layer, which is weak and wide for Sample A while a narrow full width at half-maximum (FWHM) of 46 arcsec is obtained in Sample B in which the Bi content is estimated to be 2.4% and interference fringes can be clearly seen indicating a sharp $InP_{1-x}Bi_x$/InP interface. The $InP_{1-x}Bi_x$ peak shifts to the lower angle with decreasing the growth temperature, indicating the probability of Bi atoms sticking on surface and incorporation into lattice is enhanced at low growth temperatures. As the growth temperature is further lowered to 275°C, the $InP_{1-x}Bi_x$ peak broadens.

These results reveal that growth temperature is a critical parameter to obtain smooth $InP_{1-x}Bi_x$ single crystal. The optimized growth temperature of 324°C measured by a thermo-couple is believed to be close to the Bi melting point. When the impingent Bi atoms are balanced between desorption and incorporation to lattice sites, single crystal $InP_{1-x}Bi_x$ film is achieved with no Bi droplets on the surface formed by excess Bi atoms. In addition, Bi is known to be an excellent surfactant [8], which could improve the surface and interface quality. When the

growth temperature is further decreased, excess Bi and P atoms tend to accumulate on InP deteriorating the surface and the structural quality.
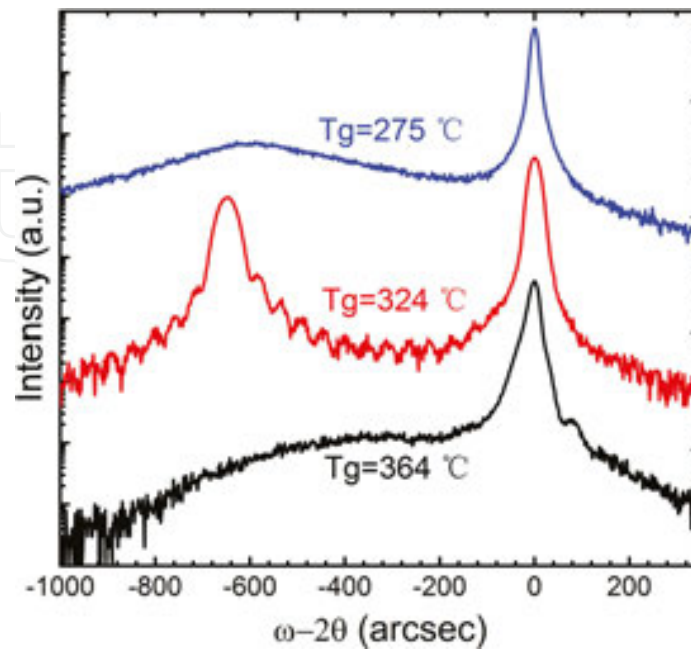

Figure 2. HRXRD (004) $\omega/2\theta$ rocking curves from $InP_{1-x}Bi_x$ samples grown at different temperatures.

2.2. Effect of Bi flux

At the optimized growth temperature, we have tried to grow $InP_{1-x}Bi_x$ using different Bi flux to check the effect of Bi flux on the growth. A set of samples were grown with Bi/In BEP ratio varied from 0 to 0.16 (0.78 μm/h, PH_3 pressure = 350 Torr). The HRXRD (004) $\omega/2\theta$ rocking curves are shown in **Figure 3(a)**, and the layer peak shifts to the lower angle when the Bi flux increases, indicating the increased incorporation of Bi in InP. **Figure 3(b)** shows the relationship between the Bi content and the FWHM of the InPBi layers and the Bi/In BEP ratio. It was found that the Bi incorporation increases linearly while the FWHM deceases for Bi concentration up to 2.4% and then broadens rapidly when further increasing the Bi flux. Both the samples with 1.8% and 2.4%, Bi has a narrow FWHM of ~50 arcsec and shows interference fringes, indicating improved composition uniformity and a smooth $InP/InP_{1-x}Bi_x$ interface.

Figure 4(a–c) shows AFM images of the $InP_{1-x}Bi_x$ with x = 0%, 1.8% and 3.0%, respectively. The RMS roughness values of the three samples are 3.9 nm, 0.7 nm and 32.6 nm, respectively, suggesting proper Bi flux can improve surface quality. As the growth temperature is very low, excessive P atoms stick on the surface, and the surface migration length of In is reduced. Thus, the InP reference sample shows a rough texture surface. With a proper Bi flux, the growth front could be covered with Bi atoms, which are commonly considered to be surfactants to improve the surface quality. However, after further increasing the Bi flux, the sample achieving 3.0% Bi incorporation exhibits a much broader diffraction line width in **Figure 3(a)**, and micrometre-scale In/Bi droplets are occurred as shown in **Figure 4(c)**, indicating Bi atoms will be accumu-

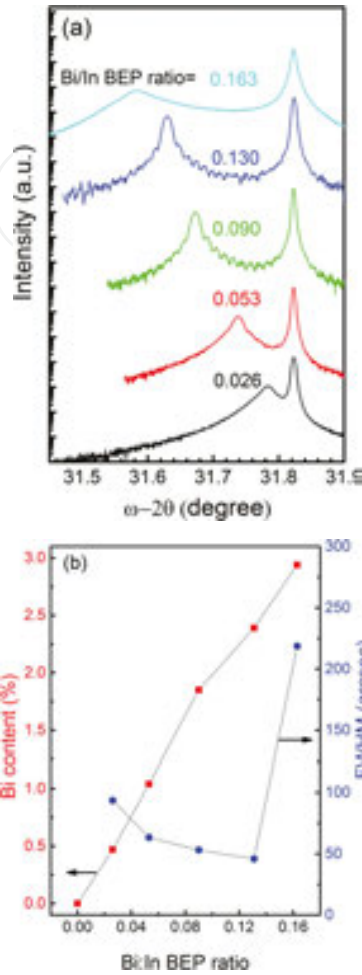lated on surface forming large metallic Bi droplets and further hinder the uniform growth of $InP_{1-x}Bi_x$.

Figure 3. (a) HRXRD (004) $\omega/2\theta$ rocking curves from $InP_{1-x}Bi_x$ samples grown at varying Bi flux; (b) dependence of the Bi content and the FWHM on Bi/In BEP ratio.

Figure 4. Surface morphology of 5×5 μm^2 InP(Bi) samples grown with different Bi flux conditions. Bi/In BEP ratio = x: 1 for (a) $x = 0$; (b) $x = 0.090$ and (c) $x = 0.163$.

2.3. Effect of PH$_3$ pressure

Normally, the growth parameter of V/III flux ratio has a direct influence on the growth of dilute bismides. In the MBE growth of a wide range of highly mismatched bismide alloys including GaAsBi, GaSbBi, InAsBi and InSbBi, a low growth temperature and near-stoichiometric growth conditions are needed to achieve efficient Bi incorporation due to the strong competition between As/Sb and Bi atoms. We have grown a set of InP$_{1-x}$Bi$_x$ layers with PH$_3$ pressure varied over a wide range from an In-rich to a P-rich condition. However, we found that the incorporation of Bi in InP is independent of the PH$_3$ pressure studied. High PH$_3$ pressure causes rough surface, and the introduction of Bi improves surface quality.
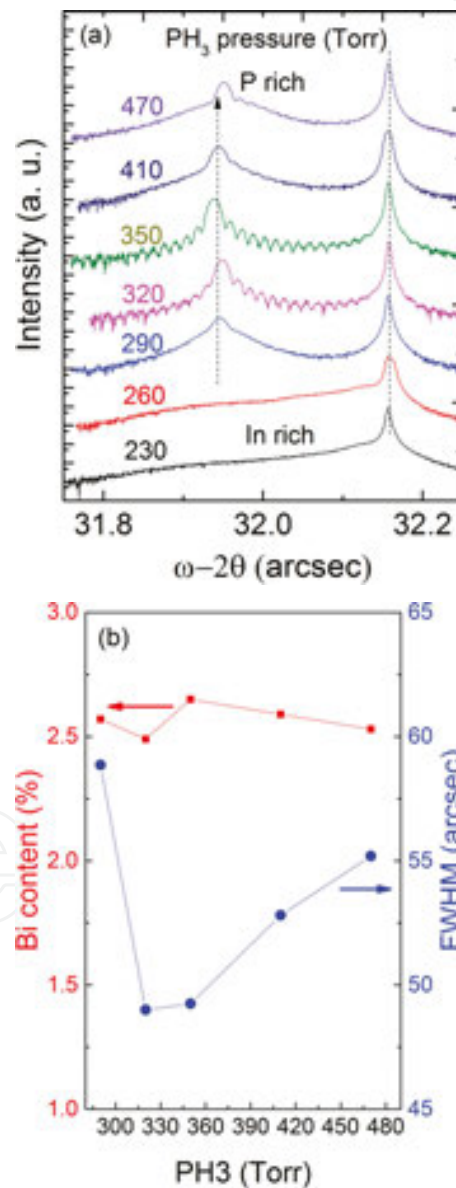

Figure 5. (a) HRXRD (004) ω/2θ rocking curves of InP$_{1-x}$Bi$_x$ layers grown at varying PH$_3$ pressures; (b) dependence of the Bi content and the FWHM on the PH$_3$ pressure.

The HRXRD (004) $\omega/2\theta$ rocking curves are shown in **Figure 5(a)**, and the effect of the PH_3 pressure on the Bi content and the FWHM is shown in **Figure 5(b)**. The PH_3 pressure of 290 Torr is near the stoichiometry threshold condition where a transition from the In-rich to the P-rich condition is expected for these samples. Under the In-rich condition, no clear epitaxial layer peak is detected by XRD measurement expected a lot of In-rich droplets on their surfaces that were examined by the AFM and EDX, indicating excess In atoms hinder the InPBi growth. For the samples grown at $PH_3 \geq 290$ Torr, i.e., under the P-rich condition, two peaks can be well seen suggesting the success of InPBi growth. Surprisingly, with increasing the PH_3 pressure, the $InP_{1-x}Bi_x$ diffraction peak fluctuates slightly while the FWHM is nearly unchanged and the interference fringes disappear. For the sample grown with the PH_3 pressure = 350 Torr, the interference fringes and a narrow FWHM of 49 arcsec are obtained, indicating an optimized III/V flux ratio to grow $InP_{1-x}Bi_x$ with sharp interface and uniform Bi incorporation.

This growth property is quite different from that in solid source MBE as well as MOCVD growth of dilute bismides mentioned before where the V elements, such as As and Sb, are commonly consider to be strong competitor of Bi, and the V to III overpressure ratio should be carefully characterized and adjusted to achieve Bi-droplet-free surfaces. The peculiar phenomenon in $InP_{1-x}Bi_x$ may be related to the group-V source used rather than the differences between the InBi and GaBi bonds.

AFM results shown in **Figure 6** reveal that with a high P to In overpressure ratio, the roughening process of the (100) InP films is mainly controlled by the number of excessive P atoms and gives rise to mountain chain-like features aligned in the (0–11) direction, leading to a relative high RMS value of 5.3 nm.
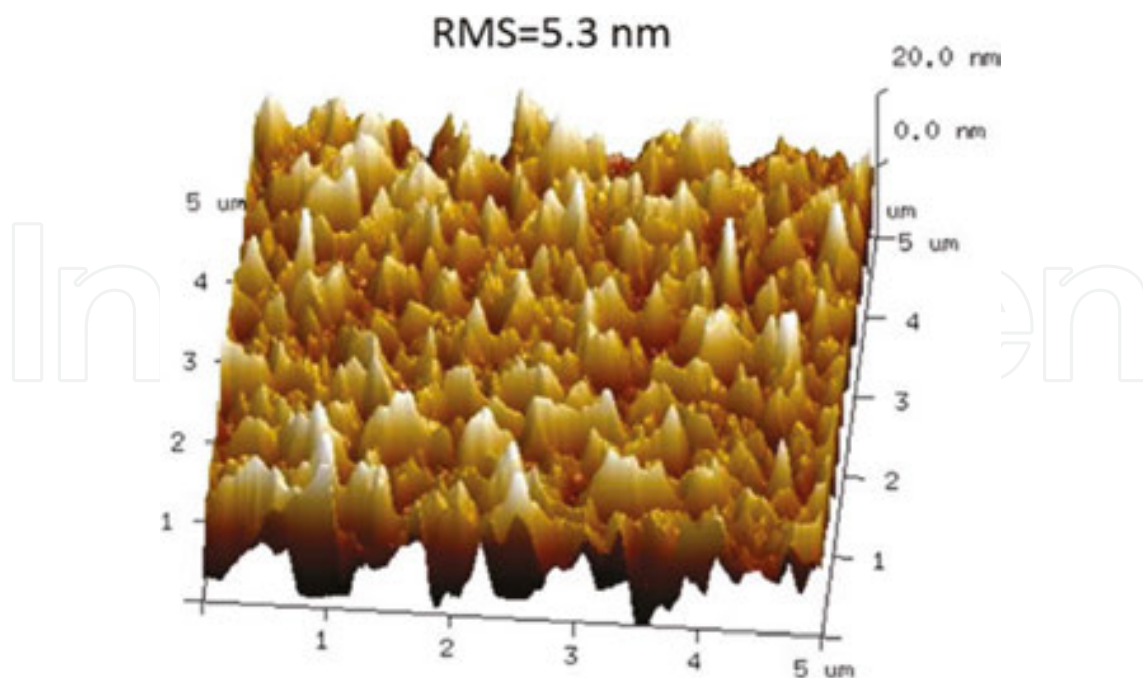

Figure 6. Surface morphology of the InP(Bi) sample grown at a relative high PH_3 pressure of 470 Torr.

2.4. Effect of growth rate

A set of 250–405 nm thick $InP_{1-x}Bi_x$ layers were grown to check the effects of growth rate varied from 0.50 to 0.81 μm/h while both the Bi flux and the PH_3 pressure were fixed. The HRXRD (004) ω/2θ rocking curves are shown in **Figure 7**. The Bi content as a function of the inverse InP growth rate is shown in **Figure 8(a)**. It is shown that the change in the Bi concentration is inversely proportional to the InP growth rate. These results indicate that Bi atoms are incorporated into the $InP_{1-x}Bi_x$ layer like dopant atoms, such as Be or Si. Be or Si has a unity sticking coefficient and the non-sensitive to the V supplies, and the doping concentration is inversely proportional to the growth rate of the host material. The $InP_{1-x}Bi_x$ sample with Bi incorporation of up to 3.7% was demonstrated at a relatively low InP growth rate of 0.50 μm/h and shows free of droplet surface (as shown in **Figure 8(b)**) and a smaller FWHM of ~105 arcsec than the sample with a Bi content up to 3.0% grown at a higher Bi flux as mentioned before, indicating the low growth rate can suppress the possibility of droplet formation and improve the uniformity of the Bi distribution. In addition, the observation of periodic elongated terraces aligned in the (0–11) direction in **Figure 8(b)** is in expectation because the P to In overpressure ratio is relatively high due to the low growth rate.
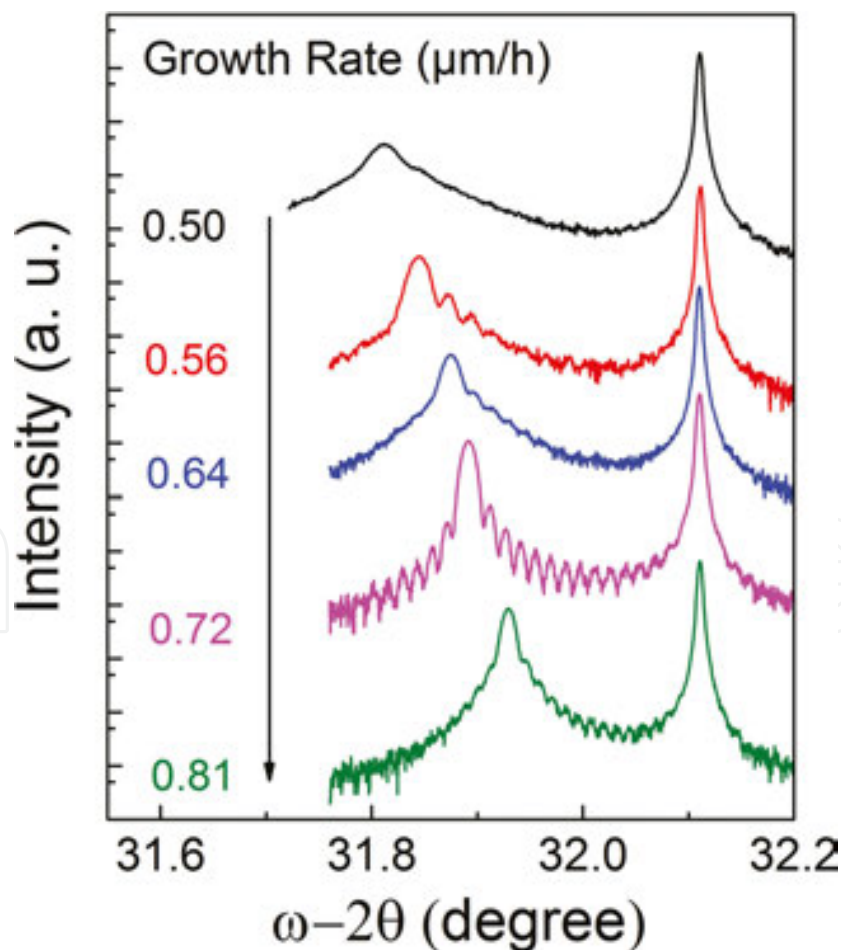

Figure 7. HRXRD (004) ω/2θ rocking curves of $InP_{1-x}Bi_x$ layers grown at varying growth rate.
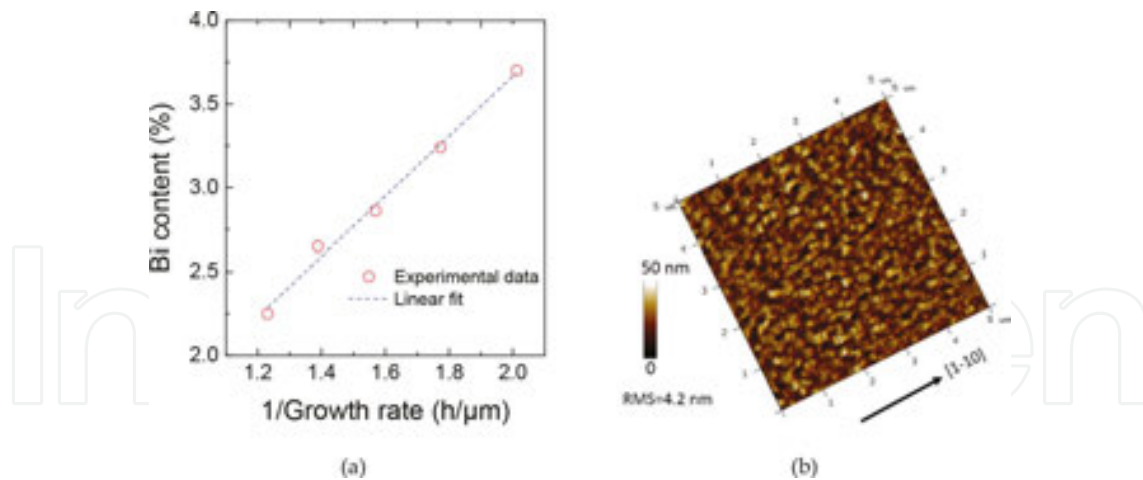
Figure 8. (a) The Bi content as a function of the inverse InP growth rate; (b) surface morphology of the InP(Bi) sample grown at a relative low InP growth rate of 0.50 μm/h.

3. Physical properties

3.1. Surface and structure properties

3.1.1. Lattice expansion

For $InP_{1-x}Bi_x$ alloy, the incorporated Bi atoms are believed to replace P atoms. Because the atom size of Bi is larger than that of P, the Bi_P replacement will cause local strain and change the lattice constant. As zinc-blende InBi has a lattice constant of 6.52 Å that is larger than InP (5.868 Å), the lattice constant of $InP_{1-x}Bi_x$ is expected to be between InBi and InP.

A 420 nm thick $InP_{1-x}Bi_x$ epilayer was grown on (100) InP substrate by GSMBE, with a 70 nm InP buffer layer grown in between to improve the initial growth surface. High-resolution XRD was performed to characterize the structural properties of $InP_{1-x}Bi_x$ films with Bi content varied from 0.47% to 3%. HRXRD (004) rocking curves in **Figure 9** show clear Pendellösung fringes, indicating the $InP_{1-x}Bi_x$ films with excellent crystal quality. All curves contain two peaks, in which the right narrow peak is from the InP substrate and the broad $InP_{1-x}Bi_x$ layer peak is located at the left side, indicating a larger lattice constant, which is in accordance with theoretical prediction. With increasing the Bi content from 0.47% to 3%, the $InP_{1-x}Bi_x$ layer peak moves to lower angles gradually. The higher the Bi content, the larger the lattice constant of $InP_{1-x}Bi_x$.

High-resolution TEM and geometric phase analysis were performed to investigate the out-of-plane (along the growth direction) strain and the in-plane (in the growth plane) strain of the epilayers to the substrate, which was performed by Dr. Minjian Wu at the Paul-Drude-Institute in Germany. **Figure 10(a)** shows the out-of-plane strain distribution. The colours in the map represent the stress intensity, in which the redder indicates a larger strain and the greener means a smaller strain. The average strain of the $InP_{1-x}Bi_x$ epilayer is about 0.60 ± 0.4%, while

the strain of InP buffer layer is $0.00 \pm 0.4\%$. The in-plane strain is $0.00 \pm 0.4\%$, which is not shown here. These results indicate that the $InP_{1-x}Bi_x$ epilayer is psudomorphically strained.
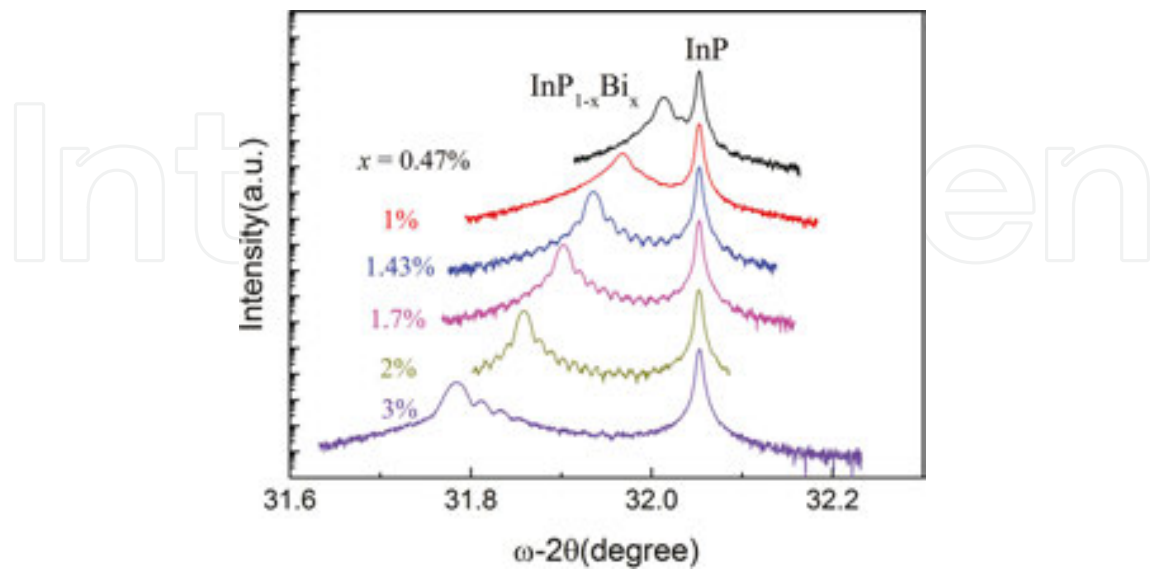

Figure 9. XRD (004) rocking curves of $InP_{1-x}Bi_x$ thin films with different Bi contents.

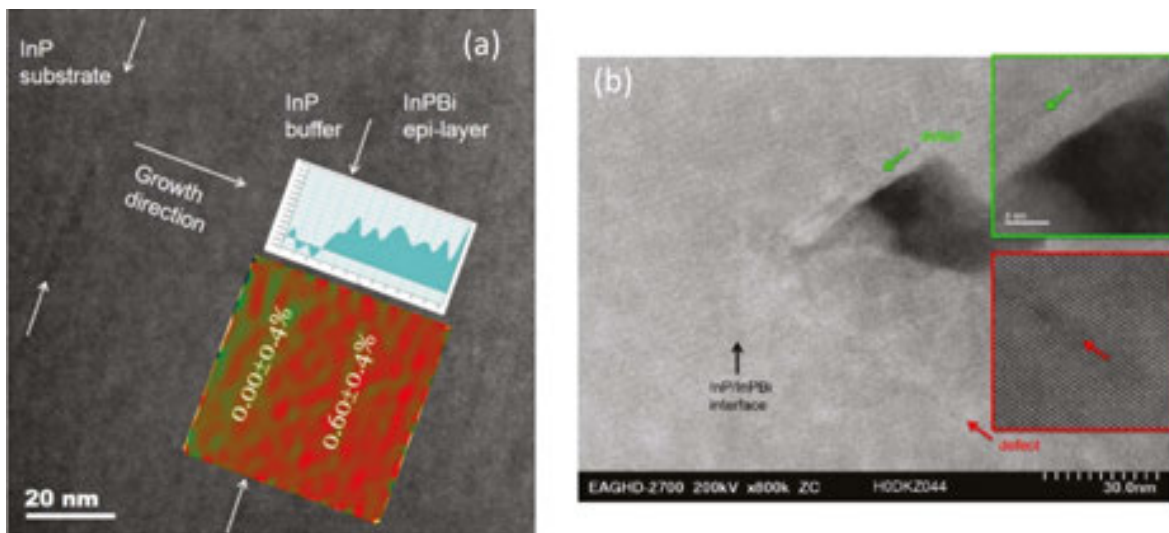**Figure 10.** (a) High resolution TEM and geometric phase analysis of $InP_{1-x}Bi_x$ layers grown on InP. (b) Cross-sectional TEM of $InP_{1-x}Bi_x$ film. The arrows in the green and red boxes point out dislocation in $InP_{1-x}Bi_x$ layer.

Figure 10(b) shows the cross-sectional TEM image of $InP_{1-x}Bi_x$ films, which were grown at a temperature of 50°C lower than that of the samples measured in **Figure 2(a)**. Dislocations are obviously seen in the region pointed out by arrows in the green and red boxes. Because of the atomic size difference between Bi and P atoms, when Bi replaces P, the surrounding atoms will be compressed. Once the stress is too large, it will relief through dislocation formation. Lattice distortion may be caused by atom substitution, vacancy and interstitial atoms.

3.1.2. Segregation

Phase separation is a general phenomenon in III-V compounds. With a large atomic radius, a large atomic mass and a low bonding energy of Bi-III, Bi segregation occurs easily in dilute bismides. This adds difficulty in MBE growth of $InP_{1-x}Bi_x$, in which a low growth temperature should be used to ensure Bi incorporation, resulting in a high tendency to defect formation.

Atom probe tomography was performed to examine the Bi distribution in $InP_{1-x}Bi_x$ thin films. A 70 nm InP buffer layer was first grown on the InP (001) substrate to improve the interface and then 420 nm $InP_{1-x}Bi_x$ was deposited on it. For sample preparation, we first coated the sample with a protective layer and pulled a wedge out, then FIB was used to form the final tip. **Figure 11** shows In, P and Bi atom distribution in the as-grown $InP_{1-x}Bi_x$ alloys. We can see four different layers. The top layer where no In, P and Bi atoms were detected was the protective layer. The lower layers are $InP_{1-x}Bi_x$ epi-layer, InP buffer layer and InP substrate in turn. The distributions of In and P atoms are quite uniform; however, Bi atoms are found to distribute somehow non-uniformity in the $InP_{1-x}Bi_x$ layer. The red arrow in **Figure 11** points out a relatively higher Bi region than the surroundings, which is an obvious evidence of Bi segregation.

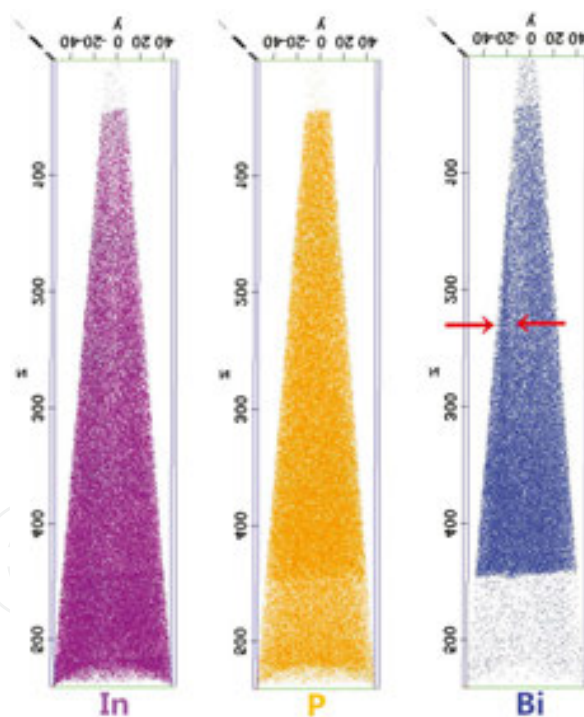**Figure 11.** Distribution map of In, P and Bi atoms in $InP_{1-x}Bi_x$ thin film deposited on an InP (001) substrate observed by atom probe tomography.

3.2. Electronic property

InPBi was predicted to be difficult to fabricate partially due to the large lattice mismatch [9]. In 2013, the success growth of $InP_{1-x}Bi_x$ has stimulated theoretical studies of this novel com-

pound further. Kopaczek *et al.* [6] have studied the band gap (E0) and spin-orbit splitting (SO) in $InP_{1-x}Bi_x$ alloys with $0 < x < 0.034$ by contactless electro-reflectance. The reduction coefficient of E0 was deduced to be 83 meV/% Bi while that of SO was 13 meV/% Bi. These results were close to the estimation in the valence band anti-crossing model and *ab initio* calculations where the shifts of E0 and SO are 106 and 20 meV/%Bi, respectively. Similarly, Bi-related band parameters were deduced theoretically by Polak *et al.* [11].

Zhang *et al.* has performed first-principle calculations systematically to investigate structural and electronic properties of the normal $InP_{1-x}Bi_x$ [12] and $In_{1-x}PBi_x$ [13] alloys, respectively. It is found that the hetero-antisite defect Bi_{In} is energetically easier than Bi_P. In $InP_{1-x}Bi_x$, the electronic states around Fermi level mainly consist of Bi-6p states, which contribute to the band gap reduction. While for $In_{1-x}PBi_x$, the Bi_{In} defect is a deep-level donor, which does not contribute to the reduction in the band gap of InP:Bi alloy but may be related to the reported strong RT PL.

3.3. Optical property

Photoluminescence (PL) and absorption measurement were carried out employing a Fourier transform infrared (FTIR) spectrometer in the rapid rather than the step-scan mode, in which a liquid-nitrogen cooled InSb detector and a CaF_2 beam splitter were used. A 532 nm laser was used as the excitation. The samples were mounted into a close-cycle refrigerator for the low temperature PL measurements.

$InP_{1-x}Bi_x$ samples of 390 nm thick and with $0\% \leq x \leq 2.49\%$ were grown directly on semi-insulating (100) InP substrates without InP buffer by V90 GSMBE system. An InP reference sample was grown under the same growth condition (LT InP) for comparison.
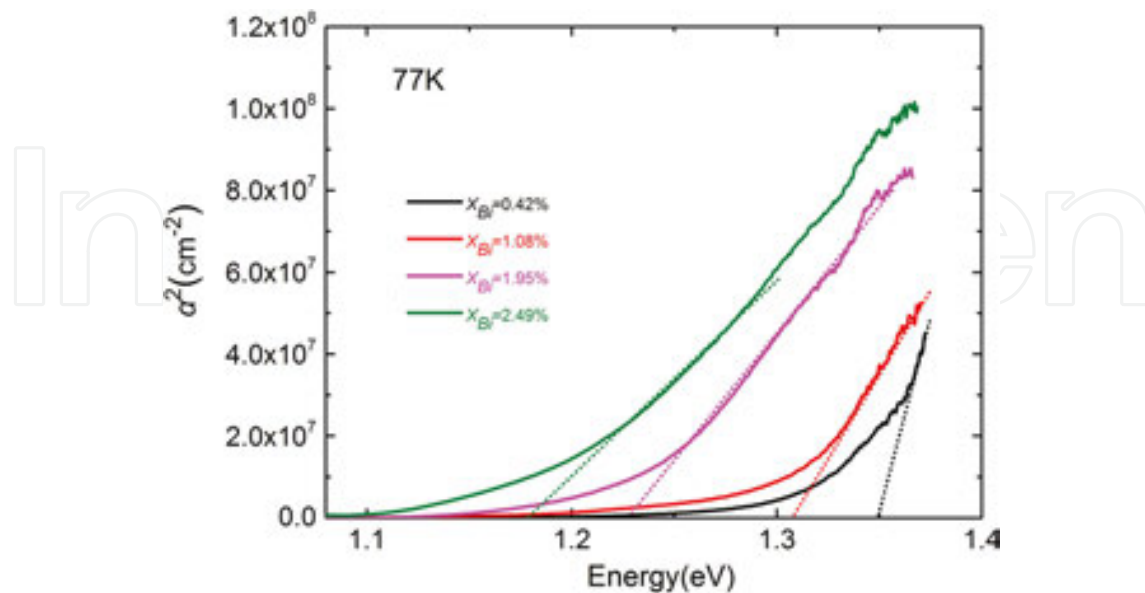

Figure 12. Square of absorption coefficient of $InP_{1-x}Bi_x$ samples with various Bi compositions as a function of photon energy at 77 K.
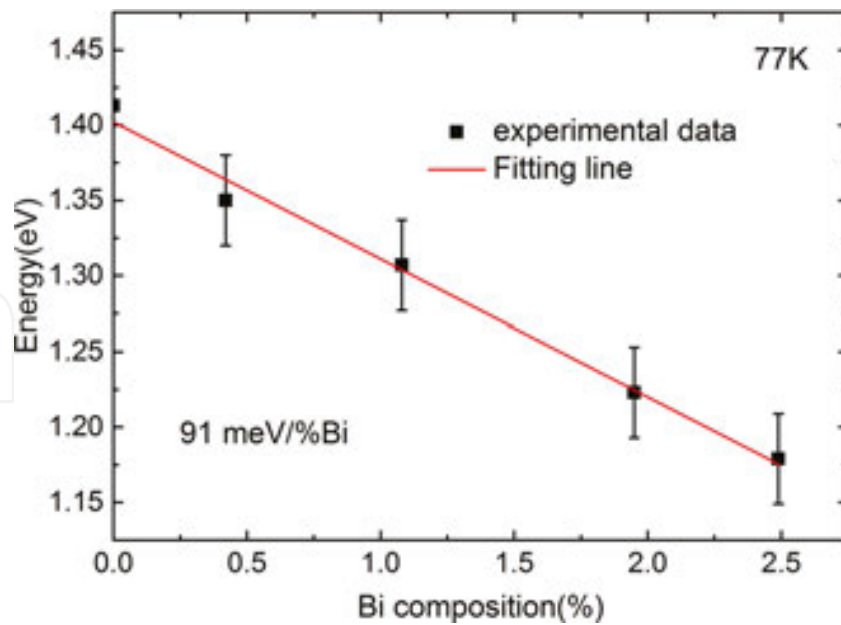
Figure 13. Band gap energy of $InP_{1-x}Bi_x$ measured from absorption spectra as a function of Bi composition. The error bars of the experimental data are labelled. The solid line is the linear fitting line of the experimental data.

Figure 12 shows square of absorption coefficient of $InP_{1-x}Bi_x$ films with various Bi compositions as a function of photon energy at 77 K. The band gap value is obtained from the linear extrapolation of the rising part for each sample. As Bi composition increases, the band edge of $InP_{1-x}Bi_x$ shifts to longer wavelengths revealing a reduction in the band gap energy. As shown in **Figure 13**, the Bi-induced band gap reduction is about 91 meV/% Bi, which is close to the measured value of 83 meV/% Bi by photoreflectance and the theoretically predicted value of 106 meV/% Bi [6].

Figure 14(a) shows PL spectra of LT InP reference sample and $InP_{1-x}Bi_x$ samples with various Bi concentrations at 10.5 K. The spectra are magnified by particular factors for visually suitable in height. Strong and broad PL peaks are observed for the samples, except for the sample with the highest Bi composition. Red arrows point to the theoretical band gap values of $InP_{1-x}Bi_x$ following the 106 meV/% Bi [6]. Blue arrows point to the band gap measured from absorption spectra as shown in **Figure 13**. In general, the PL emission features shift to lower energy with increasing Bi concentration as expected, and the spectral line shape also changes. The LT InP reference spectrum manifests two sharp peaks at about 1.42 eV and 1.39 eV, respectively, superimposed by a broad peak centred at about 1.3–1.35 eV. Compared to that of the InP grown at the same condition, the $InP_{1-x}Bi_x$ samples have totally different PL characteristic. In all cases, the observed PL signals show peak energies much smaller than the band gap of $InP_{1-x}Bi_x$ as shown by the arrows in **Figure 14(a)**. When only doping with 0.42% Bi, a strong and broad feature appears at about 1.05 eV and becomes a dominant signature in the PL spectra. As Bi content increases to 1.95%, the PL intensity begins to decrease, and a new feature at around 0.8 eV emerges. Overall, the $InP_{1-x}Bi_x$ PL spectral evolution versus Bi concentration shows that features at high energy gradually quench and features at low energy emerge. Such anomalous

PL behaviours are different from those found in GaAsBi [4] and GaSbBi [14] where PL peak follows the band gap reduction for a small amount of incorporated Bi composition.
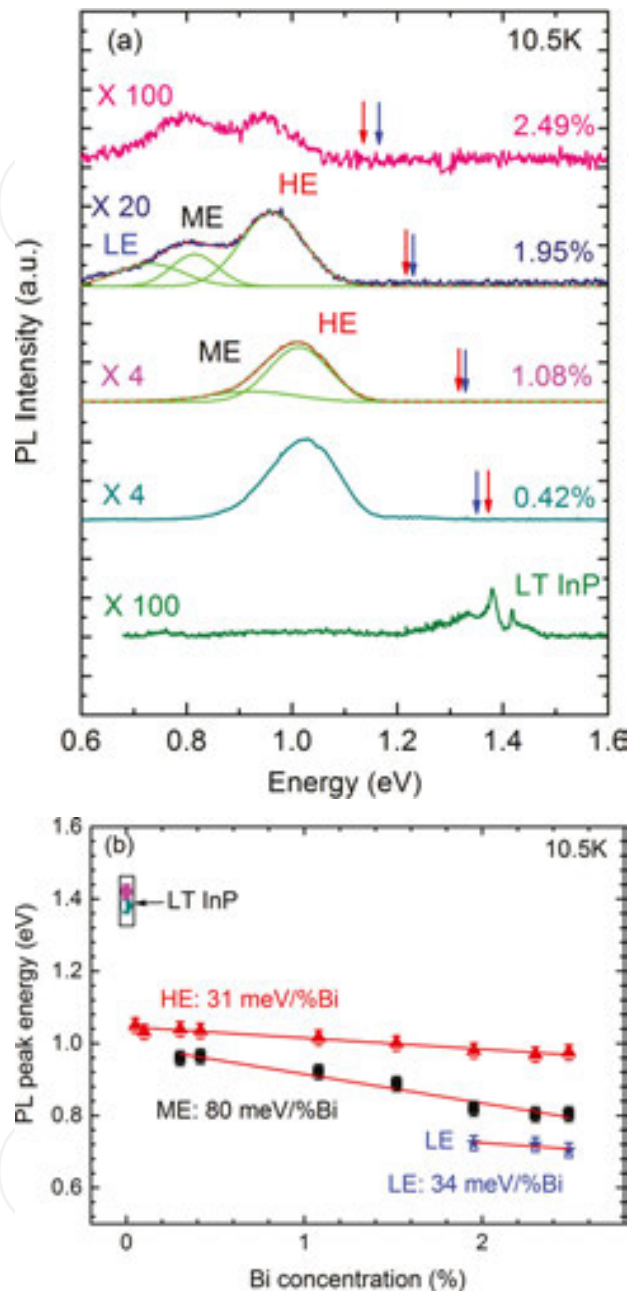

Figure 14. (a) PL spectra of $InP_{1-x}Bi_x$ samples with various Bi concentrations and LT InP reference sample at 10.5 K. Red arrows point to the theoretical band gap values of $InP_{1-x}Bi_x$ following the 106 meV/% Bi. Blue arrows point to the band gap measured from absorption spectra following the 91 meV/% Bi. The green curves are the Gaussian peak fitting. The red solid curve is the sum of the fitted lines. (b) PL peak energy evolution versus Bi concentration. The red solid line is a linear fit of HE (slope = 31 meV/% Bi); the black solid line is a linear fit of ME (slope = 80 meV/% Bi); the blue solid line is a linear fit of LE (slope = 34 meV/% Bi).

The broad and asymmetry PL peaks of $InP_{1-x}Bi_x$ can be well fitted by three features and labelled by low energy (LE), medium energy (ME) and high energy (HE). **Figure 14(a)** shows a typical

fitted PL spectrum of $InP_{1-x}Bi_x$ with x = 1.95%. Both HE and ME peaks exist almost in all $InP_{1-x}Bi_x$ PL spectra and are dominant, while the LE peak is resolved only for samples with x ≥ 1.95%. As shown in **Figure 14(b)**, the HE emission is found to monotonically decrease with Bi concentration from 1.05 eV down to 0.98 eV and shifts at ~31 meV/% Bi. The ME emission is found to monotonically decrease with Bi concentration from 0.95 eV down to 0.80 eV and shifts at ~80 meV/% Bi. Recent theoretical calculations by Kopaczek *et al*. reveal that the conductive band (CB) shift is 27 meV/% Bi and the VB shift is 79 meV/% Bi in $InP_{1-x}Bi_x$ [6]. Considering the HE and ME shifts versus Bi concentration are close to the CB and VB shifts, respectively, we attribute the HE transition to electrons in the CB of $InP_{1-x}Bi_x$ recombining with holes trapped at a deep level, and the ME transition to electrons trapped at a deep level to holes in the VB of $InP_{1-x}Bi_x$.

To determine the nature of $InP_{1-x}Bi_x$ PL and verify the existence of deep levels, we performed deep level transient spectroscopy (DLTS) measurements on the LT InP reference and $InP_{1-x}Bi_x$ (x = 2.49 %) grown on n + InP substrates. From the DLTS results, two deep levels with the ionization energy of the n-type deep level to be 0.38 eV below the CB edge and the p-type deep level to be 0.31 eV above the VB maximum of InP, respectively, are identified. Based on the PL spectra and the DLTS results, the physical origins of HE, ME and LE can be explained as follows: (1) HE is related to the transition between conductive band (CB) and the p-type deep level. (2) ME is related to the transition between the n-type deep level and valence band (VB). (3) LE is related to the transition between the n-type deep level and the p-type deep level. The 0.38 eV donor-like deep level is likely related to the intrinsic deep level in LT grown InP [15]. This level is considered to originate from the intrinsic antisite of P_{In}. While the VB of $InP_{1-x}Bi_x$ results from the anti-crossing of the Bi impurity level with the VB of InP, we attribute the p-type deep level to the formation of Bi pairs or complex Bi-related clusters. It has been theoretically shown that Bi pairs in GaP:Bi can form a series of energy levels above the VB [16]. The energy difference from the VB edge increases with decrease in the Bi pair distance and can reach as deep as 0.5 eV [16]. This is also expected in InP:Bi because the Bi impurity level is slightly below the VB edge of InP [3].

The PL intensity is found to significantly increase by Bi incorporation due to the effective spatial trapping of holes, which is a positive indication for light-emitting devices. Detailed analysis of $InP_{1-x}Bi_x$ PL has explained the origin of the strong light emission.

3.4. Electrical and transport properties

Electrical and transport measurements and first-principle calculations have been combined to investigate the dependence of electric properties of $InP_{1-x}Bi_x$ on Bi content [17]. Data of Hall effect measurements at variable temperatures for undoped $InP_{1-x}Bi_x$ show a high electron concentration in the order of 10^{18} cm^{-3}. The interesting thing is that both the electron concentration and the mobility have a nonlinear relationship with the Bi content. The electron concentration first decreases with increasing incorporated Bi content from 0% to 1.83% and then increases with keep on increasing Bi after its content exceeds to 1.83%. However, the electron mobility shows quite an inverse variation in that of the electron concentration as a function of Bi content.

P_{In} antisites and V_P vacancies are dominant donors in InP and $InP_{1-x}Bi_x$. Chen *et al.* found a level of 0.23 eV below conduction band minimum (CBM) and a level 0.12 eV above CBM hypothetically corresponding to P_{In} level and V_P level [18], respectively, in which the P_{In} level does not accord with our experimental results as shown in Section 3.3. V_P and P_{In} concentration dominates the electron concentration at low Bi content ($x < 1.83\%$) and high Bi content ($x > 1.83\%$), respectively. When Bi content is below 1.83%, the increasing incorporated Bi will occupy more V_P vacancies, decreasing the V_P concentration and impurity scattering, thus causing the decrease in electron concentration and the increase in electron mobility. After Bi content exceeds to 1.83%, both P_{In} and V_P density increases with increase in the Bi content, enlarging the overall electron concentration and reducing the electron mobility (**Figure 15**).
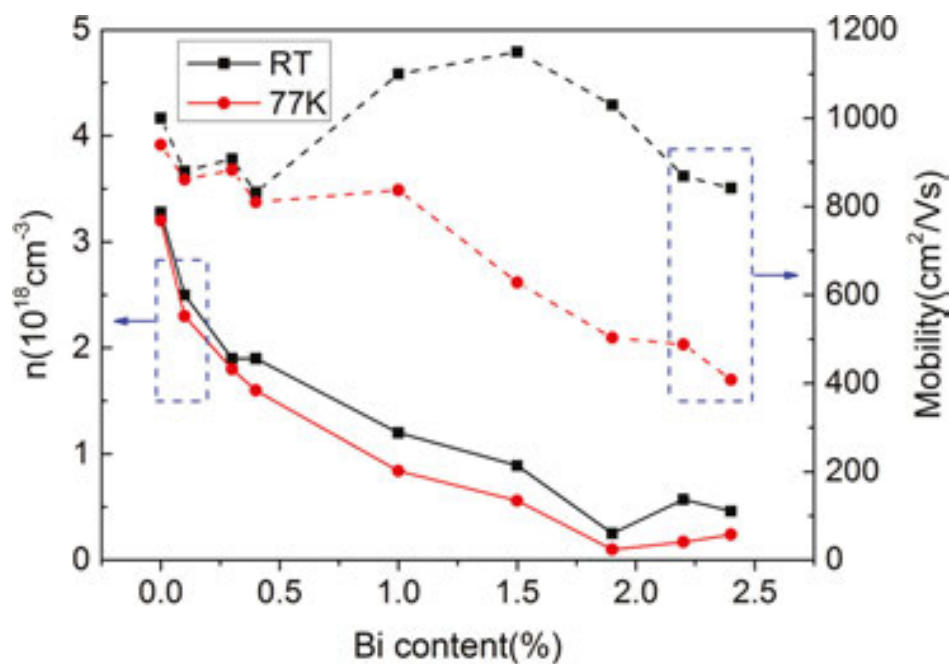

Figure 15. The relationship of electron concentration and mobility with Bi content at room temperature and 77 K.

4. Annealing

In this section, a systematic study on the effect of annealing on the structural and optical properties of $InP_{1-x}Bi_x$ is presented [19]. The 390 nm thick $InP_{1-x}Bi_x$ sample was diced into small pieces and annealed for 2 min at different temperatures ranging from 400°C to 800°C. To prevent P decomposition during annealing, the samples were capped with an InP substrate.

Figure 16(a) and **(b)** shows HRXRD (115) $\omega/2\theta$ rocking curves of the as-grown and annealed $InP_{0.981}Bi_{0.019}$ layer and the extracted Bi content along with strain relaxation from four asymmetric (11±5) rocking curves, respectively. The rocking curve of the as-grown $InP_{1-x}Bi_x$ shows a narrow peak with a FWHM of only 71 arcsec, revealing high crystal quality. As the annealing temperature is raised to 400°C, the FWHM slightly increases to 84 arcsec. Further increasing

annealing temperature broadens the line width. This is attributed to enhanced strain relaxation as shown in **Figure 16(b)**. The Bi content hardly changes with the annealing temperature rising up to 500°C, indicating a good stability of this material. However, when the annealing temperature increases to 600°C, the FWHM suddenly deteriorates to 161 arcsec and the diffraction peak in HRXRD shifts to a higher angle. The Bi content of InPBi annealed at 600°C is distinctly decreased comparing to that annealed at 500°C, which is similar to InGaAsBi annealed up to 650°C [20]. As the annealing temperature keeps on ascending to 700°C, the FWHM increases to 215 arcsec. Meanwhile, the diffraction peak further moves towards higher angles with the intensity dropping drastically. From **Figure 16(b)**, the Bi content decreases to 0.0165. As the annealing temperature increases to 800°C, no accurate peak position can be extracted owing to a very broad signal. This suggests the deterioration of crystal structure under high annealing temperatures. The trend of peak shifting towards high angles implies that the average Bi content continuously decreases, which is indicated by the black dashed line in **Figure 16(b)**.
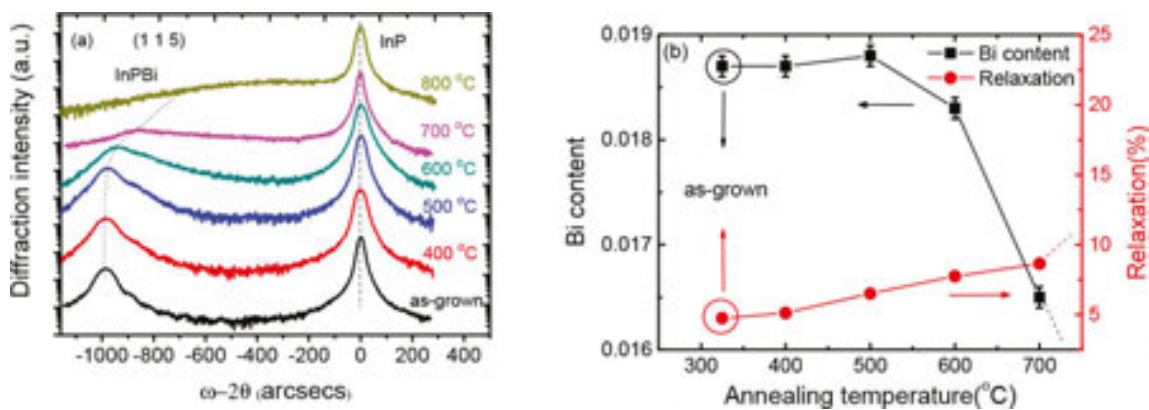

Figure 16. (a) HRXRD (004) $\omega/2\theta$ rocking curves of $InP_{1-x}Bi_x$ samples with various annealing temperatures. (b) The extracted Bi content of $InP_{1-x}Bi_x$ before and after annealing at different temperatures.

The III-Bi bonding energy is small because Bi atom has a very large atomic radius compared with other group V elements. Thus, annealing at high temperatures likely causes Bi outdiffusion from $InP_{1-x}Bi_x$ leading to decrease in the Bi content. However, the measured temperature for initial Bi outdiffusion of $InP_{1-x}Bi_x$ is about 600°C, which is lower than GaAsBi (800°C) [21]. Considering the bond energy of Ga-Bi (158.6 ± 16.7 kJ/mol) is larger than In-Bi (153.6 ± 1.7 kJ/mol) [22], Bi is expected to be more stable in GaAsBi.

Room temperature PL spectra of $InP_{0.981}Bi_{0.019}$ and LT InP before and after annealing at different temperatures are shown in **Figure 17(a)**. For a visually suitable PL peak height, the spectra were magnified by particular factors. The wide PL signals can be fitted very well by three peaks, which are marked by LE, ME and HE, respectively. When the annealing temperature is below 500°C, broad PL spectra with similar figures are observed in the energy range from 0.45 to 1.1 eV. The dominant peak is ME with relative weak intensities for both LE and HE peak. As shown in **Figure 17(b)**, the normalized integrated PL intensity increases when compared with the as-grown one. When the annealing temperature rises to 400°C, a maximum PL enhance-

ment by 20% is obtained and the PL spectrum is essentially unchanged. This result is encouraging as optical quality can be improved without compromising the PL peak energy shift. As shown in **Figure 17(b)**, when the annealing temperature is below 500°C, the integrated PL intensity of the LT InP reference sample decreases with increasing annealing temperature. This suggests that the PL improvement is mainly attributed to the removal of Bi-related defects similar to the circumstance of annealing on InPN [23].
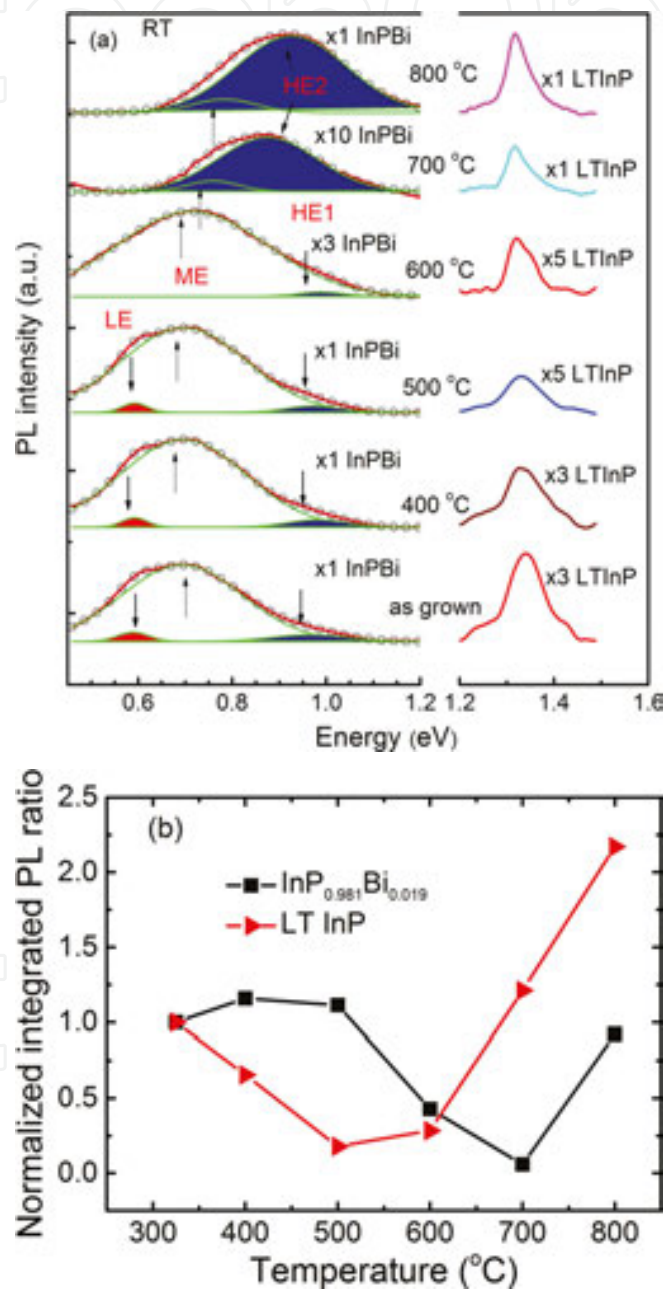

Figure 17. (a) PL spectra of $InP_{1-x}Bi_x$ (x = 0.019) and LT grown InP as reference at room temperature. The dotted lines are measured data. The green and red lines are the Gaussian peak fitting and the sum of fitted lines, respectively. (b) The normalized integrated PL intensity in respect of the intensity from the non-annealed sample as a function of the annealing temperature.

5. Quaternary phosphide bismides

Ternary alloy InGaP is an essential material for red laser diodes [22], while InAlP is an active material for nitride-free yellow-green photoelectric devices and has potential application in laser diodes, light-emitting diodes, displayers and multi-junction solar cells [24–26]. Incorporating Bi into InGa(Al)P is expected to reduce the band gap to tune the emission wavelength to longer range and improve the temperature sensitivity of InGa(Al)P lasers. Meanwhile, the strain of InGa(Al)PBi can be tuned freely from tensile to compressive by adjusting Bi and In/Ga(Al) contents.

5.1. InGaPBi thin films

InGaPBi thin films have been grown on GaAs and InP substrates using GSMBE [27, 28].The growth temperature is crucial for Bi incorporation, and the optimized temperature for InGaPBi growth on InP and GaAs substrates is 280°C and 300°C, respectively. The Bi content increased from 0.5% to 2.2% by increasing the Bi flux. A 330 nm thick $In_{0.468}Ga_{0.532}P_{1-x}Bi_x$ films were grown on GaAs substrates with Bi content of 0.5%, 1.0% and 1.8%, respectively. A 370 nm thick $In_{0.975}Ga_{0.025}P_{1-x}Bi_x$ films were grown on InP substrates with Bi content of 0.42%, 1.6% and 2.2%, respectively. InGaP reference samples were also grown for comparison.

HRXRD (004) rocking curves show clear Pendellösung fringes as shown in **Figure 18(a)** and **(b)**, indicating excellent crystal and interface quality. The strain of InGaPBi films can be tuned from tensile to compressive by increasing the Bi content. The HRXRD $\omega/2\theta$ rocking curves on the (004) crystal plane and asymmetric (115) reflections were performed to obtain the exact lattice mismatch. The FWHM of the epilayer peak for all the InGaPBi films on GaAs substrate is very small, 54.2, 49.2 and 49.9 arcsec for $In_{0.468}Ga_{0.532}P_{1-x}Bi_x$ films with 0.5%, 1.0% and 1.8% Bi content, respectively, indicating good crystal quality. For the reference $In_{0.468}Ga_{0.532}P$ film on GaAs substrate, the lattice constant is 5.646 Å with −1378 ppm negative mismatch to the GaAs substrate. As expected, with increasing the Bi content from 0.5% to 1.8%, the diffraction peak moves to smaller angles. The lattice mismatch between the InGaPBi sample with Bi content of 0.5% and 1.0% with the GaAs substrate is −810 and −314 ppm, respectively. As the Bi content is increased up to 1.8%, the InGaPBi epilayer is compressively strained to the GaAs substrate with a mismatch of 598 ppm. Through this method, InGaPBi films have been successfully grown on GaAs with controllable strain from tensile to compressive. For the $In_{0.975}Ga_{0.025}P_{1-x}Bi_x$ films grown on InP substrate with x = 0%, 0.42%, 1.6% and 2.2%, the mismatch to InP is tuned from −1776 to −1189, 338 and 1093 ppm, respectively. The strain of $In_{0.975}Ga_{0.025}P_{1-x}Bi_x$ films on InP can also be tuned from tensile to compressive.

Surface morphology characterized by AFM [27, 28] indicates that Bi has little effect on the InGaPBi surface grown on a GaAs substrate but can smoothen the InGaP(Bi) samples grown on an InP substrate. Weak room temperature PL was observed at 1.78 eV for the InGaPBi films on GaAs with a Bi content of 0.5%, featuring near band optical transition with 122 meV smaller than that of InGaP. For all the InGaPBi films on InP, room temperature PL shows strong and broad light emission at energy levels much smaller than the InP band gap.
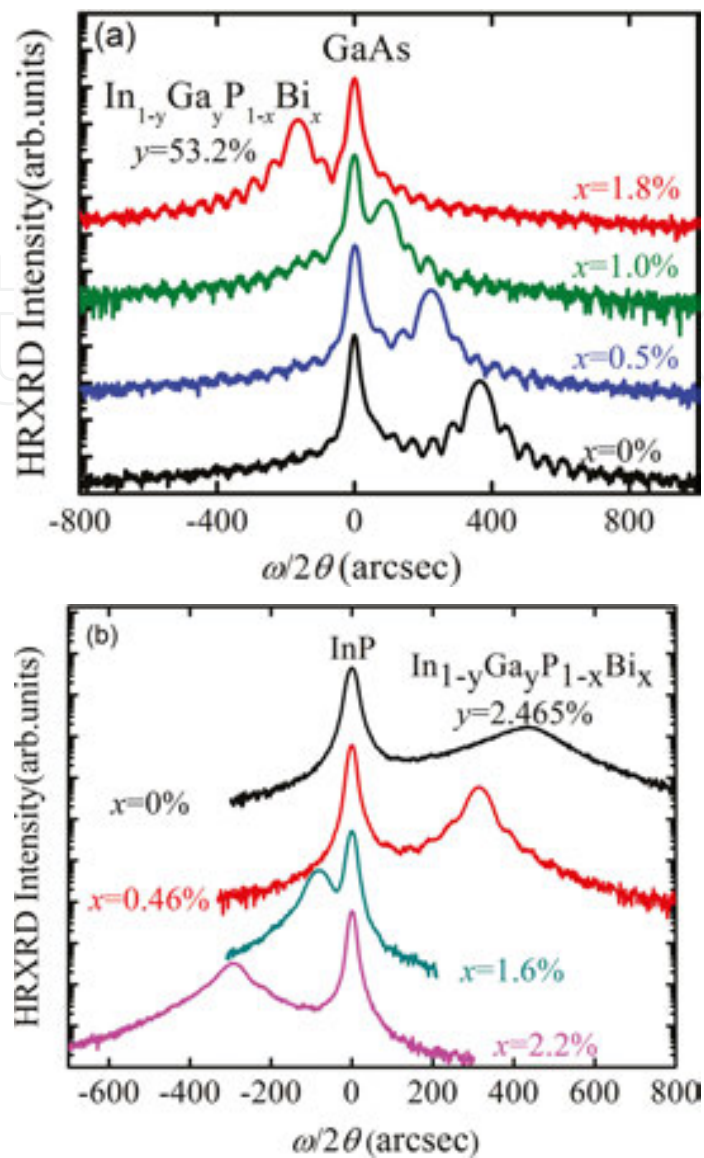
Figure 18. XRD rocking curves of InGaPBi films on (a) GaAs and (b) InP.

5.2. InAlPBi thin films

$In_{1-y}Al_yP_{1-x}Bi_x$ thin films on GaAs with Bi concentration up to $x = 1.6\%$ were grown by GSMBE. The growth temperature is critical for Bi incorporation, and the growth temperature window is quite small around the optimal temperature at 300°C. After surface deoxidation, a 100 nm undoped GaAs buffer layer was grown at 580°C and then decreases the substrate temperature to 300°C to grow the InAlPBi epilayer with a thickness of 360 nm. The pressure of the P_2 flux was kept at 350 Torr during the InAlPBi epilayer growth. Keeping the same In/Ga ratio, the temperature of the Bi cell was set between 427°C and 462°C, respectively.

Rutherford backscattering spectrometry (RBS) was performed for the InAlPBi sample with 1.6% Bi content to determine Bi composition and confirms that 93% of Bi atoms are located at

substitutional sites. The surface morphology was characterized using AFM. From the 2×2 μm^2 scan image of the InAlPBi samples, the RMS roughness is only 0.5 nm, revealing that all the samples have smooth surfaces.

The lattice quality was characterized using the HRXRD ω/2θ rocking curves both on the (004) crystal plane and on the asymmetric (115) reflections. $In_{1-y}Al_yP_{1-x}Bi_x$ thin films reveal excellent structural quality and perfect interfaces. The FWHMs of the epilayer peak of the InAlPBi samples are 48.2, 46.5 and 49.2 arcsec, respectively, for the samples with Bi content of 0.5%, 0.8% and 1.6%, indicating good crystal quality. For the $In_{0.467}Al_{0.533}P$ reference sample and the InAlPBi samples with 0.5% and 1.6% Bi contents, the lattice mismatch with GaAs substrate is −695, −318 and 1041 ppm, respectively. The strain can be tuned from tensile to compressive by increasing Bi contents. The corresponding strain relaxation is 0.6%, 1.6% and 1.1%, respectively. That is, all the InAlPBi films are almost strained.

6. Potential device application

Modern medical diagnostic technology tends to adopt non-invasive painless technique, such as ultrasound examination, X-ray photography, X-ray computer tomography and nuclear magnetic resonance technology. Some diagnosis technology can offer 3D images; however, the spatial resolution is limited in hundreds of micro-metres. Optical coherence tomography (OCT) is one of the non-invasive painless diagnosis techniques developed in recent years [29–31], which could offer higher resolution comparing with other diagnosis techniques. Basically, it is an interferometric technique. A typical OCT system uses a Michelson interferometer with a white light or low coherence light source. Light is split into the reference mirror and sample, respectively, and reclaimed to interfere. The interference signals will be collected by the photo detector and analysed by computer to extract the information out of the biological tissues (**Figure 19**).

The spatial resolution (Δl) of OCT technique is inversely proportional to the line width of the spectrum of the light source in the following formula [29]:

$$\Delta l = 0.44 \lambda_0^2 / \Delta\lambda \qquad (1)$$

λ_0 and $\Delta\lambda$ are the centric wavelength and FWHM of the light source, respectively. The wider the FWHM, the higher the spatial resolution. So, a wide-spectrum light source is preferred in the OCT system. Currently, the most popular light source used in a commercial OCT system is super-luminescence diode [29], with which the best spatial imaging resolution is around 10 μm. To get even higher resolution, we need to use a light source with a wider spectrum.

$InP_{1-x}Bi_x$ shows strong room temperature PL, which is eight times stronger in the peak intensity and 80 times stronger in the integrated PL intensity than that of InP grown under the same conditions. The spectrum is broad from 1.4 to 2.7 μm, and the widest shows a FWHM of 690 nm. If we use $InP_{1-x}Bi_x$ to fabricate super-luminescence diodes and apply them in the OCT

system, the spatial resolution could be improved to 1.5 µm theoretically. It should be noted that $InP_{1-x}Bi_x$ thin films were first realized by MBE just in 2013 [6], the physical properties are still under investigation. If we further optimize the epitaxial growth parameters and tailor the material structure, it is promising to further broaden the FWHM of the room temperature PL or to blue shift the central PL wavelength while keeping the current FWHM. This will improve the spatial resolution of OCT system beyond a psychological value of 1 µm, thus significantly advancing the development of OCT diagnosis technique.
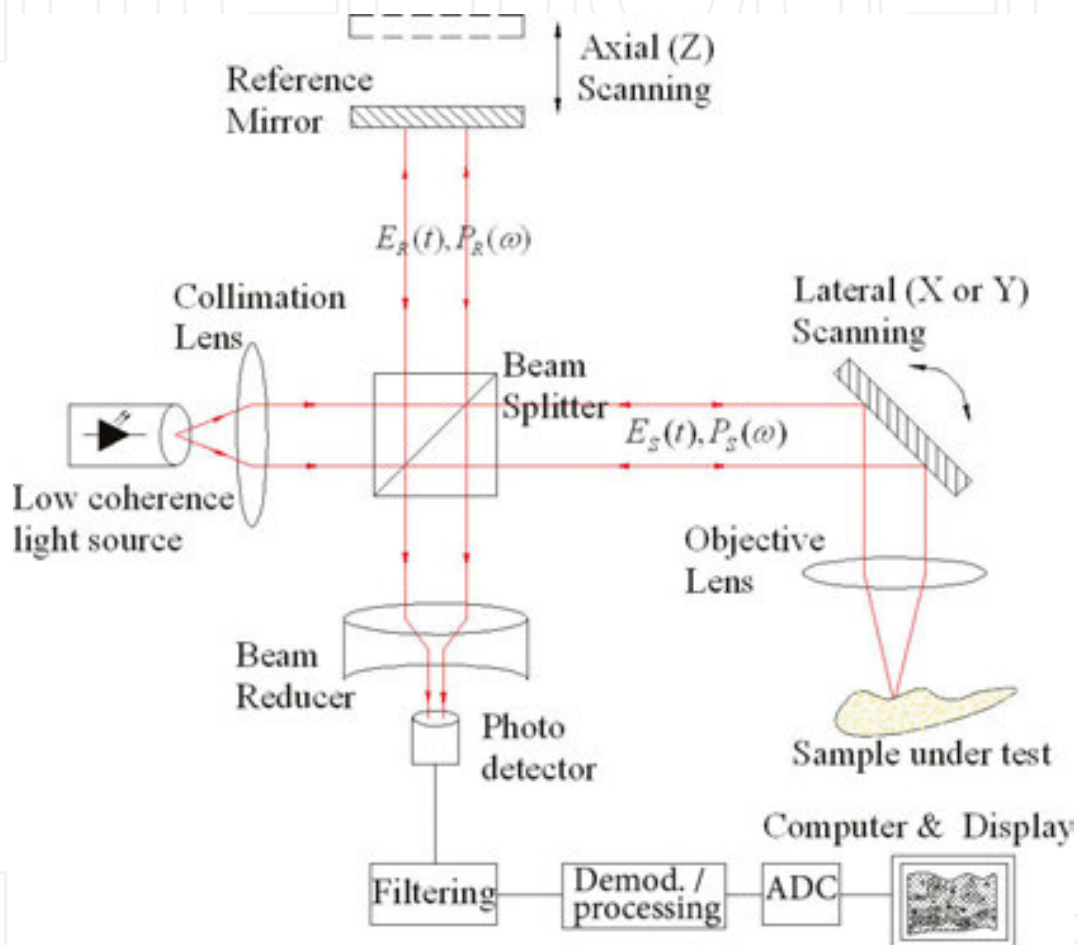

Figure 19. A typical optical setup of single point OCT system [32].

7. Summary

In this chapter, we have reviewed the MBE growth and characterization of $InP_{1-x}Bi_x$ and its quaternary alloys InGaPBi and InAlPBi. To get a high Bi content while maintaining good crystal quality is challenging because of the small growth window for $InP_{1-x}Bi_x$. Growth parameters were investigated in detail to find an appropriate growth window. Annealing is performed to study Bi thermal stability and influence on the physical properties of $InP_{1-x}Bi_x$. The optical

property of $InP_{1-x}Bi_x$ is distinctive comparing with other dilute bismides and shows broad and strong PL at room temperature. This makes $InP_{1-x}Bi_x$ a potential candidate for fabricating super-luminescence diodes applicable in OCT with spatial resolution in the nanometre regime.

Author details

Liyao Zhang[1], Wenwu Pan[1], Xiaoyan Wu[1], Li Yue[1] and Shumin Wang[1,2*]

*Address all correspondence to: shumin@mail.sim.ac.cn

1 State Key Laboratory of Functional Materials for Informatics, Shanghai Institute of Microsystem and Information Technology, CAS, Shanghai, China

2 Department of Microtechnology and Nanoscience, Chalmers University of Technology, Gothenburg, Sweden

References

[1] Oe, K. and H. Okamoto, New semiconductor alloy $GaAs_{1-x}Bi_x$ grown by metal organic vapor phase epitaxy. Japanese Journal of Applied Physics, 1998. 37(11A): p. L1283.

[2] Tixier, S., M. Adamcyk, T. Tiedje, S. Francoeur, A. Mascarenhas, P. Wei, et al., Molecular beam epitaxy growth of $GaAs_{1-x}Bi_x$. Applied Physics Letters, 2003. 82(14): p. 2245–2247.

[3] Alberi, K., J. Wu, W. Walukiewicz, K. Yu, O. Dubon, S. Watkins, et al., Valence-band anticrossing in mismatched III-V semiconductor alloys. Physical Review B, 2007. 75(4): p. 045203.

[4] Fluegel, B., S. Francoeur, A. Mascarenhas, S. Tixier, E. Young, and T. Tiedje, Giant spin-orbit bowing in $GaAs_{1-x}Bi_x$. Physical Review Letters, 2006. 97(6): p. 067205.

[5] Francoeur, S., M.-J. Seong, A. Mascarenhas, S. Tixier, M. Adamcyk, and T. Tiedje, Band gap of $GaAs_{1-x}Bi_x$, $0 < x < 3.6\%$. Applied Physics Letters, 2003. 82(22): p. 3874–3876.

[6] Kopaczek, J., R. Kudrawiec, M. Polak, P. Scharoch, M. Birkett, T. Veal, et al., Contactless electroreflectance and theoretical studies of band gap and spin-orbit splitting in $InP_{1-x}Bi_x$ dilute bismide with $x \leq 0.034$. Applied Physics Letters, 2014. 105(22): p. 222104.

[7] Pan, W., P. Wang, X. Wu, K. Wang, J. Cui, L. Yue, et al., Growth and material properties of InPBi thin films using gas source molecular beam epitaxy. Journal of Alloys and Compounds, 2016. 656: p. 777–783.

[8] Naceur, H.B., T. Mzoughi, I. Moussa, L. Nguyen, A. Rebey, and B. El Jani, Surfactant effect of bismuth in atmospheric pressure MOVPE growth of InAs layers on (100) GaAs

substrates. Physica E: Low-dimensional Systems and Nanostructures, 2010. 43(1): p. 106–110.

[9] Berding, M.A., A. Sher, A.B. Chen, and W. Miller, Structural properties of bismuth-bearing semiconductor alloys. Journal of Applied Physics, 1988. 63(1): p. 107–115.

[10] Wang, K., Y. Gu, H. Zhou, L. Zhang, C. Kang, M. Wu, et al., InPBi single crystals grown by molecular beam epitaxy. Scientific Reports, 2014. 4.

[11] Polak, M., P. Scharoch, and R. Kudrawiec, First-principles calculations of bismuth induced changes in the band structure of dilute Ga–V–Bi and In–V–Bi alloys: chemical trends versus experimental data. Semiconductor Science and Technology, 2015. 30(9): p. 094001.

[12] Zhang, X., P. Lu, L. Han, Z. Yu, J. Chen, and S. Wang, Structural and electronic properties of InPBi alloys. Modern Physics Letters B, 2014. 28(17): p. 1450140.

[13] Wu, L., P. Lu, C. Yang, D. Liang, C. Zhang, and S. Wang, The effect of Bi In hetero-antisite defects in $In_{1-x}PBi_x$ alloy. Journal of Alloys and Compounds, 2016. 674: p. 21–25.

[14] Rajpalke, M.K., W.M. Linhart, M. Birkett, K.M. Yu, J. Alaria, J. Kopaczek, et al., High Bi content GaSbBi alloys. Journal of Applied Physics, 2014. 116(4): p. 043511.

[15] Liang, B.W., P.Z. Lee, D.W. Shih, and C.W. Tu, Electrical-properties of inp grown by gas-source molecular-beam epitaxy at low-temperature. Applied Physics Letters, 1992. 60(17): p. 2104–2106.

[16] Usman, M., C.A. Broderick, A. Lindsay, and E.P. O'Reilly, Tight-binding analysis of the electronic structure of dilute bismide alloys of GaP and GaAs. Physical Review B, 2011. 84(24).

[17] Wei, G., D. Xing, Q. Feng, W. Luo, Y. Li, K. Wang, et al., The identification of the dominant donors in low temperature grown InPBi materials. arXiv preprint arXiv: 1603.09015, 2016.

[18] Chen, W.M., P. Dreszer, A. Prasad, A. Kurpiewski, W. Walukiewicz, E.R. Weber, et al., Title: origin of [ital n]-type conductivity of low-temperature grown InP. Journal of Applied Physics, 1994. 76: p. 1.

[19] Wu, X.Y., K. Wang, W.W. Pan, P. Wang, Y.Y. Li, Y.X. Song, et al., Effect of rapid thermal annealing on $InP_{1-x}Bi_x$ grown by molecular beam epitaxy. Semiconductor Science and Technology, 2015. 30(9).

[20] Ye, H., Y.X. Song, Y. Gu, and S.M. Wang, Light emission from InGaAs:Bi/GaAs quantum wells at 1.3 mu m. Aip Advances, 2012. 2(4).

[21] Mohmad, A.R., F. Bastiman, C.J. Hunter, R. Richards, S.J. Sweeney, J.S. Ng, et al., Effects of rapid thermal annealing on $GaAs_{1-x}Bi_x$ alloys. Applied Physics Letters, 2012. 101(1).

[22] Ishikawa, M., Y. Ohba, H. Sugawara, M. Yamamoto, and T. Nakanisi, Room-temperature cw operation of InGaP/InGaAlP visible light laser diodes on GaAs substrates

grown by metalorganic chemical vapor deposition. Applied Physics Letters, 1986. 48(3): p. 207–208.

[23] Umeno, K., Y. Furukawa, N. Urakami, S. Mitsuyoshi, H. Yonezu, A. Wakahara, et al., Growth and luminescence characterization of dilute InPN alloys grown by molecular beam epitaxy. Journal of Vacuum Science & Technology B: Microelectronics and Nanometer Structures, 2010. 28(3): p. C3B22.

[24] Bour, D., J. Shealy, G. Wicks, and W. Schaff, Optical properties of AlxIn$_{1-x}$P grown by organometallic vapor phase epitaxy. Applied Physics Letters, 1987. 50(10): p. 615–617.

[25] Mukherjee, K., D. Beaton, T. Christian, E. Jones, K. Alberi, A. Mascarenhas, et al., Growth, microstructure, and luminescent properties of direct-bandgap InAlP on relaxed InGaAs on GaAs substrates. Journal of Applied Physics, 2013. 113(18): p. 183518.

[26] Schneider, Jr, R. and J. Lott, InAIP/InAlGaP distributed Bragg reflectors for visible vertical cavity surface-emitting lasers. Applied Physics Letters, 1993. 62(22): p. 2748–2750.

[27] Wang, K., P. Wang, W. Pan, X. Wu, L. Yue, Q. Gong, et al., Growth of semiconductor alloy InGaPBi on InP by molecular beam epitaxy. Semiconductor Science and Technology, 2015. 30(9): p. 094006.

[28] Yue, L., P. Wang, K. Wang, X. Wu, W. Pan, Y. Li, et al., Novel InGaPBi single crystal grown by molecular beam epitaxy. Applied Physics Express, 2015. 8(4): p. 041201.

[29] Fercher, A.F., W. Drexler, C.K. Hitzenberger, and T. Lasser, Optical coherence tomography-principles and applications. Reports on Progress in Physics, 2003. 66(2): p. 239.

[30] Huang, D., E.A. Swanson, C.P. Lin, J.S. Schuman, W.G. Stinson, W. Chang, et al., Optical coherence tomography. Science, 1991. 254(5035): p. 1178–1181.

[31] Schmitt, J.M., Optical coherence tomography (OCT): a review. IEEE Journal of Selected Topics in Quantum Electronics, 1999. 5(4): p. 1205–1215.

[32] Pumpkinegan. Optical coherence tomography. 2006 [An image depicting a single point optical coherence tomography system]. Available from: https://en.wikipedia.org/wiki/Optical_coherence_tomography.